Journal of Power Sources 379 (2018) 278–287

Contents lists available at ScienceDirect

Journal of Power Sources

journal homepage: www.elsevier.com/locate/jpowsour

Scalable synthesis of $NiMoO_4$ microspheres with numerous empty nanovoids as an advanced anode material for Li-ion batteries

Jin-Sung Park[a], Jung Sang Cho[b], Yun Chan Kang[a,*]

[a] Department of Materials Science and Engineering, Korea University, Anam-Dong, Seongbuk-Gu, Seoul, 136-713, Republic of Korea
[b] Department of Engineering Chemistry, Chungbuk National University, Chungbuk, 361-763, Republic of Korea

HIGHLIGHTS

- $NiMoO_4$ microspheres with empty nanovoids are produced by spray-drying process.
- Uniquity of structure enables longer cycle life and higher quality performances.
- $NiMoO_4$ microspheres exhibit excellent characteristics for Li-ion batteries.

GRAPHICAL ABSTRACT

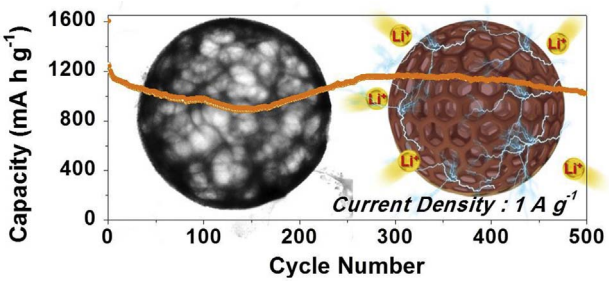

ARTICLE INFO

Keywords:
Nanostructured material
Carbon composite
Spray drying
Lithium secondary battery

ABSTRACT

Closely in line with advances in next-generation energy storage materials, anode materials for lithium-ion batteries (LIBs) with high capacity and long cycle life have been widely explored. As part of the current effort, nickel molybdate ($NiMoO_4$) microspheres with empty nanovoids are synthesized via spray drying process and subsequent one-step calcination in air. Dextrin in the atomized droplet is phase segregated during the spray drying process and calcined in air atmosphere, resulting in numerous empty nanovoids well-distributed within a microsphere. The empty nanovoids alleviate volume expansion during cycling, shorten lithium-ion diffusion length, and facilitate contact between electrode and electrolyte materials. Along with the high discharge capacity of $NiMoO_4$ material, as high as 1240 mA h g^{-1} for the 2nd cycle at a high current density of 1 A g^{-1}, uniquity of the structure enables longer cycle life and higher quality performances. The discharge capacity corresponding to the 500th cycle is 1020 mA h g^{-1} and the capacity retention calculated from the 2nd cycle is 82%. In addition, a discharge capacity of 413 mA g^{-1} is obtained at an extremely high current density of 10 A g^{-1}.

1. Introduction

With the continuously surging demand for eco-friendly and sustainable energy supplies, lithium ion batteries (LIBs) have received tremendous attention worldwide and are currently the dominant power source for portable electronic devices [1–22]. However, for lithium ion batteries to be used in large-scale energy applications, such as low-emission electric vehicles, further improvements in terms of capacity and rate capability are needed [1–9]. The design of advanced anode materials with optimum composition for lithium ion batteries is considered critical to achieving high electrochemical performance [10–18]. Transition metal molybdates are promising candidates for electrode materials for LIBs in view of their high capacity due to a variety of reversible reduction/oxidation activities resulting from multiple

* Corresponding author.
E-mail address: yckang@korea.ac.kr (Y.C. Kang).

https://doi.org/10.1016/j.jpowsour.2018.01.050
Received 27 June 2017; Received in revised form 17 January 2018; Accepted 19 January 2018

valence states [12–18]. Particularly, $NiMoO_4$ has received considerable attention owing to the high electrochemical performance of nickel ion and comparatively high electrical conductivity of molybdenum [16–18]. Unfortunately, selecting the right material alone is insufficient for designing optimum electrode materials due to repetitive volume changes during the lithiation/delithiation process, resulting in rapid capacity fading [16–21]. Material architecture of a highly effective surface that accommodates volume expansion is a powerful tool for enhancing battery performance [16–21].

The introduction of empty nanovoids within a microsphere has greatly improved electrochemical performance, despite the fact that the volumetric capacity is impaired due to the empty space [22–27]. Recently, Wang et al. synthesized mesoporous Fe_2O_3 spherical particles by spray pyrolysis with mesopores providing additional voids that alleviate structural stress during electrochemical reaction [26]. They allowed shorter lithium ion diffusion pathway, ensuring high rate performance. Cho et al. synthesized multiroom-structured Co_3O_4 microspheres by a spray pyrolysis process using hydrophilic dextrin, without applying template nanobeads, and proved the effectiveness of empty nanovoids in LIBs [27]. Inspired by these researches, spray drying method was adopted to synthesize microspheres with empty nanovoids for application in anode materials for LIBs. To the best of our knowledge, multiroom-structured microspheres applied as anode material for LIBs have not been synthesized by spray drying process. Spray drying is commonly used for large-scale production of spherical microspheres [28–32].

We herein report a facile synthesis method for transition metal molybdate oxide microspheres with empty nanovoids. Notably, nanovoids within the microspheres could be introduced without the use of surfactant or removable hard templates. A pilot-scale spray drying process and subsequent heat treatment in air formed empty nanovoids by decomposition and combustion of phase-segregated dextrin. The lithium ion storage performance of the multiroom-structured $NiMoO_4$ microsphere with empty nanovoids is compared with its counterpart, a $NiMoO_4$ microsphere prepared from a spray solution without dextrin via an identical process. Along with the high capacity of multi-component transition metal oxide material, long cycle life up to 500 cycles was achieved for the $NiMoO_4$ microspheres, owing to the structural merits of tens of empty nanovoids distributed within the microspheres.

2. Experimental

2.1. Sample preparation

The $NiMoO_4$ microspheres with empty nanovoids were synthesized via a spray drying process and subsequent calcination step in air. The pilot-scale spray drying system shown in Fig. S1 was used to prepare the dense spherical microspheres. The spray drying solution was prepared by dissolving 0.075 M $(NH_4)_6Mo_7O_{24}{\cdot}4H_2O$ (98%, Daejung), 0.075 M $Ni(NO_3)_2{\cdot}H_2O$ (98%, Sigma Aldrich), and 40 g L^{-1} of dextrin [$(C_6H_{10}O_5)_n$, Samchun] in distilled water. After vigorous stirring, the homogeneous solution was pumped to a two-fluid nozzle and then atomized at a pressure of 2.0 bar. Spray dryer inlet and outlet temperatures were adjusted to 300 °C and 120 °C, respectively. The spray-dried microspheres were consecutively loaded onto an alumina boat and placed in a quartz tube reactor and heated to 300, 400, and 500 °C at a rate of 10 °C min^{-1} under air atmosphere.

2.2. Characterization techniques

The morphologies of the prepared microspheres were observed using field emission scanning electron microscopy (FE-SEM; Hitachi, S-4800) and field emission transmission electron microscopy (FE-TEM; JEOL, JEM-2100F). Crystallographic analysis was performed at the Korea Basic Science Institute (Daegu) via X-ray diffraction (XRD; X'Pert PRO MPD) using Cu-Kα radiation (λ = 1.5418 Å). X-ray photoelectron spectroscopy (XPS; Thermo Scientific K-Alpha) with focused monochromatic Al-Kα radiation at 12 kV and 20 mA was used to determine the compositions of the specimens. The surface areas of the microspheres were determined using the Brunauer–Emmett–Teller (BET) method with N_2 as the adsorbate gas. Thermogravimetric analysis (TGA) was performed with a Pyris 1 TGA (Perkin Elmer, temperature range = 25–800 °C, heating rate = 10 °C min^{-1}, static air atmosphere) instrument.

2.3. Electrochemical measurements

The electrochemical properties of the prepared microspheres were analyzed by constructing 2032-type coin cells. The anode was prepared by mixing the active material, carbon black, and sodium carboxymethyl cellulose (CMC) in a weight ratio of 7:2:1. Li metal was used as the counter-electrode and microporous polypropylene film was used as the separator. The electrolyte was produced by dissolving 1 M $LiPF_6$ in a mixture of fluoroethylene carbonate/dimethyl carbonate (FEC/DMC; 1:1 v/v). The discharge/charge characteristics of the samples were investigated by cycling over a potential range of 0.001–3 V at various current densities. Cyclic voltammograms were acquired at a scan rate of 0.1 mV s^{-1}. The dimensions of the negative electrode containing the microspheres were 1 cm × 1 cm with a mass loading of approximately 1.2 mg cm^{-2}. The electrochemical impedance was measured over a frequency range of 0.01 Hz–100 kHz via electrochemical impedance spectroscopy (EIS).

3. Results and discussion

The formation mechanism of empty nanovoids constituting the multiroom-structured $NiMoO_4$ microsphere prepared from the spray drying process and subsequent oxidation is illustrated in Scheme 1. Each atomized droplet was dried and formed microspheres comprising ammonium molybdate, nickel nitrate, and dextrin. SEM images of the spray-dried product with dense structure are shown in Fig. S2. Dextrin was phase-segregated during the spray drying process and subsequent oxidation caused dextrin decomposition, yielding the $NiMoO_4$/C or $NiMoO_4$ microspheres with empty nanovoids, depending on the post-treatment temperatures.

The morphologies of the $NiMoO_4$/C microspheres (denoted as $NiMoO_4$/C-A3) formed by oxidation of the spray-dried product at 300 °C are shown in Fig. 1. The SEM and TEM images in Fig. 1a and b revealed the microspheres with spherical shape and non-aggregation characteristics. Fractured microspheres in the magnified SEM image in Fig. 1a and TEM image in Fig. 1b–d clarify the nanorooms constituting the multiroom-structured microspheres. The TEM image presented in Fig. 1d shows the close-up framework of the microsphere. Ultrafine nanocrystals were embedded in the amorphous carbon matrix, which restricted the growth of $NiMoO_4$ crystallites, and thus were hardly distinguishable from the TEM image. The high resolution TEM image shown in Fig. 1e shows a lattice fringe separated by 2.05 Å which is, using the Bragg's law, calculated as 44.1° in the JCPDS card #12-0348. The selected area electron diffraction (SAED) pattern shown in Fig. 1f further elucidates the crystal structure of $NiMoO_4$. The d-spacing values of 2.48, 2.05, and 1.52 Å are calculated as 36.2, 44.1, and 60.7°, respectively, in the JCPDS card #12-0348. Unfortunately, the crystal planes corresponding to the d-spacing values are undefined to the best of our knowledge. Elemental dot mapping images shown in Fig. 1g revealed uniformly distributed Ni, Mo, and C throughout the multiroom-structured microsphere. Carbon remaining within the structure was confirmative, for the oxidation temperature was not high enough.

The morphologies of the multiroom-structured $NiMoO_4$ microspheres oxidized at 400 °C (denoted as $NiMoO_4$-A4) and 500 °C (denoted as $NiMoO_4$-A5) are shown in Figs. 2 and 3, respectively. $NiMoO_4$-A4 and $NiMoO_4$-A5 microspheres share similar morphologies with $NiMoO_4$/C-A3. However, individual nanocrystal was clearly seen from

Scheme 1. Formation mechanism of $NiMoO_4$ microspheres with numerous empty nanovoids.

the close-up TEM images shown in Figs. 2d and 3d. Combustion of carbon in the $NiMoO_4$/C composite microspheres explicitly revealed the $NiMoO_4$ nanocrystals constituting the multiroom-structured microsphere. The high resolution TEM images shown in Figs. 2e and 3e show lattice fringes separated by 3.78 and 3.35 Å calculated as the 23.5 and 26.6° in the JCPDS #12-0348, respectively. Both SAED patterns of $NiMoO_4$-A4 and $NiMoO_4$-A5, which are shown in Figs. 2f and 3f, respectively show the d-spacing values of 6.70, 3.35, and 2.30 Å, which are calculated as 13.2, 26.6, and 39.1° in the JCPDS #12-0348. Elemental dot mapping images shown in Figs. 2g and 3g revealed that carbon in the $NiMoO_4$/C composite microspheres was eliminated when oxidized at 400 and 500 °C, respectively. The theoretical density of $NiMoO_4$ material is known as 3.37 g cm^{-3}. However, the density of multiroom-structured $NiMoO_4$-A4 microspheres calculated from the specific pore volume was low as 1.96 g cm^{-3}. The phase and crystallinity of multiroom-structured $NiMoO_4$ and $NiMoO_4$/C microspheres oxidized at various temperatures were analyzed by X-ray diffraction (XRD) pattern, as shown in Fig. S3. The peaks of the XRD patterns were in accordance with $NiMoO_4$ phase (JCPDS #12-0348) irrespective of oxidation temperatures. However, the $NiMoO_4$/C composite microspheres had broad $NiMoO_4$ phase peaks. Amorphous carbon and a low oxidation temperature of 300 °C resulted in the $NiMoO_4$/C composite microspheres with low crystallinity, as confirmed by TEM images in Fig. 1. The mean sizes of nanocrystallites comprising $NiMoO_4$-A4 and $NiMoO_4$-A5 microspheres calculated by Scherrer's equation were 15.8 and 20.0 nm, respectively.

The chemical nature of the $NiMoO_4$ microspheres oxidized at 400 °C was characterized via X-ray photoelectron spectra (XPS). In the Ni 2p spectrum shown in Fig. 4a, two major peaks corresponding to Ni $2p_{3/2}$ and Ni $2p_{1/2}$ doublets and their satellite peaks could be clearly observed. The Ni $2p_{3/2}$ peak could be deconvoluted into two peaks at 856.1 and 858.7 eV confirming the oxidation states of nickel: Ni^{2+} and Ni^{3+}, respectively [33,34]. Analogously, deconvolution of the high resolution Ni $2p_{1/2}$ XPS spectrum consists of two peaks at binding energies of 874.1 and 876.5 eV, each corresponding to Ni^{2+} and Ni^{3+}, respectively [33,34]. In the Mo 3d spectrum of the microspheres (Fig. 4b), two peaks at binding energies of 232.3 and 235.4 eV were attributed to Mo $3d_{5/2}$ and Mo $3d_{3/2}$, respectively, characterizing Mo^{6+} [35,36]. The O 1s spectrum shown in Fig. 4c was deconvoluted into two apparent peaks. The first peak at a binding energy of 530.5 eV can be assigned to metal-oxygen bond, whereas the second peak at 531.8 eV is relevant to the oxygen ions with a low coordination number at the surface, consistent with the reference value [17,35,36]. The brief quantitative summary of oxidation states of nickel and molybdenum calculated from XPS spectra was added in the supporting information as Table S1. The ratio of Ni^{2+} to Ni^{3+} was calculated as 81:19. The existence of Ni^{3+} could be attributed to surface oxidation of Ni nanocrystals [33]. Thermogravimetric (TG) analysis was used to determine the existence and amount of carbon in $NiMoO_4$/C-A3 and $NiMoO_4$-A4 microspheres. The TG curve of $NiMoO_4$/C-A3 microspheres shown in Fig. S4a suggests a two-step weight loss below 800 °C. Evaporation of adsorbed water molecules was responsible for the weight loss below 120 °C. The steep weight loss between 430 and 510 °C was associated with combustion of amorphous carbon, which amounted for approximately 16 wt%. The TG curve of $NiMoO_4$-A4 microspheres in Fig. S4b confirmed the complete elimination of amorphous carbon during oxidation at 400 °C for 3 h. The measured BET surface areas of $NiMoO_4$/C-A3, $NiMoO_4$-A4, and $NiMoO_4$-A5 microspheres were 15, 33, and 31 $m^2 g^{-1}$, respectively. The combustion of amorphous carbon increased the BET surface area of the microspheres. The N_2 absorption/desorption isotherms in Fig. S5a and BJH pore size distributions in Fig. S5b confirmed that the $NiMoO_4$-A4 and $NiMoO_4$-A5 microspheres consisted mainly of mesopores. The mesopores of the two samples primarily originated from the pores between the $NiMoO_4$ nanocrystals formed by combustion of amorphous carbon. The crystal growth at 500 °C decreased the BET surface area and pore volume of the $NiMoO_4$-A5 microspheres.

The electrochemical properties of the multiroom-structured $NiMoO_4$ microspheres are presented in Figs. 5 and 6. Fig. 5a–c display cyclic voltammetry (CV) curves of the multiroom-structured $NiMoO_4$/C and

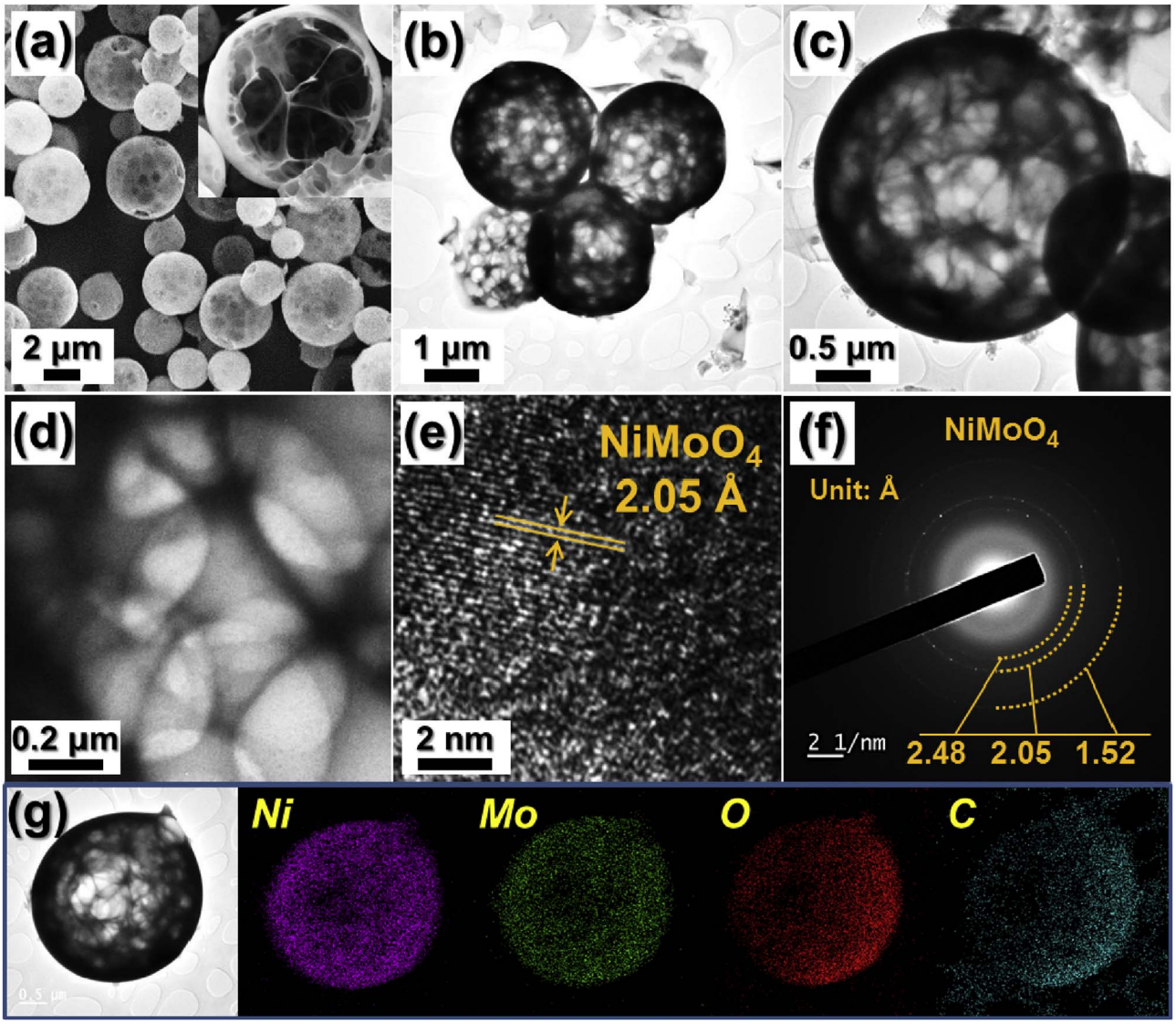

Fig. 1. Morphologies, SAED, and elemental mapping images of the multiroom-structured $NiMoO_4$/C microspheres obtained at a post-treatment temperature of 300 °C: (a) SEM image, (b–d) TEM images, (e) HR-TEM image, (f) SAED pattern, and (g) elemental mapping images.

$NiMoO_4$ microspheres oxidized at various temperatures obtained over potential range of 0.001–3 V (vs. Li/Li^+) for the first 5 cycles at a scan rate of 0.1 mV s^{-1}. A reduction peak located at 1.3 V in $NiMoO_4$/C-A3 and 1.6 V in $NiMoO_4$-A4 and $NiMoO_4$-A5 in the first cathodic sweep could be assigned to the formation of a solid-electrolyte interface (SEI) layer [18,37]. Peaks located at 0.60, 0.35, and 0.1 V in the first cathodic scan correspond to the reduction of $NiMoO_4$ into nanosize metallic Ni and Mo [16,17,38,39]. Equation (1) states the relevant electrochemical equation. Two peaks at 1.4 and 1.8 V in the first anodic scan correspond to the oxidation of metallic Ni and Mo to Ni^{2+} and Mo^{6+}, respectively (Equations (2) and (3)) [18,38,39]. In the following cycles, two pairs of redox peaks at 1.8/1.3 and 1.4/0.7 V could be allocated to the oxidation/reduction reaction of MoO_3 and NiO and the reaction can be stated as in Equation (4) [18,33,37–39]. The shapes of the CV curves are almost identical from the 2nd cycle, proving the stable electrochemical performance of the $NiMoO_4$/C and $NiMoO_4$ microspheres. Combining the CV analysis of $NiMoO_4$ multiroom-structured microspheres and previously reported $NiMoO_4$ materials, the electrochemical conversion reaction of $NiMoO_4$ could be summarized as follows [16–18]:

$$NiMoO_4 + 8Li^+ + 8e^- \rightarrow Ni + Mo + 4Li_2O \quad (1)$$

$$Ni + Li_2O \rightarrow NiO + 2Li^+ + 2e^- \quad (2)$$

$$Mo + 3Li_2O \rightarrow MoO_3 + 6Li^+ + 6e^- \quad (3)$$

$$NiO + MoO_3 + 8Li^+ + 8e^- \leftrightarrow Ni + Mo + 4Li_2O \quad (4)$$

The charge and discharge profiles of the $NiMoO_4$/C and $NiMoO_4$ microspheres for the 1st and 2nd cycles at a current density of 1 A g^{-1} are shown in Fig. 6a and b, respectively. They coincided well with the CV curves in that distinct plateaus appeared at 1.3 V for $NiMoO_4$/C and at 1.6 V for $NiMoO_4$ microspheres, which are assigned to the formation of the SEI layer in the initial discharging step. The initial discharge capacities of $NiMoO_4$/C-A3, $NiMoO_4$-A4, and $NiMoO_4$-A5 microspheres were 1654, 1605, and 1362 mA h g^{-1}, respectively, and the corresponding initial Coulombic efficiencies were 73, 78, and 80%, respectively. $NiMoO_4$/C-A3 microspheres exhibited the lowest initial Coulombic efficiency due to a certain degree of initial irreversible capacity loss caused by amorphous carbon material.

The cycling performances of the $NiMoO_4$/C and $NiMoO_4$ microspheres at a current density of 1 A g^{-1} are shown in Fig. 6c, in which the first discharge capacities are not shown. The discharge capacities of the $NiMoO_4$/C-A3, $NiMoO_4$-A4, and $NiMoO_4$-A5 microspheres at the 500th cycle were 740, 1020, and 424 mA h g^{-1}, respectively, and the capacity retentions measured from the second cycle were 64, 82, and

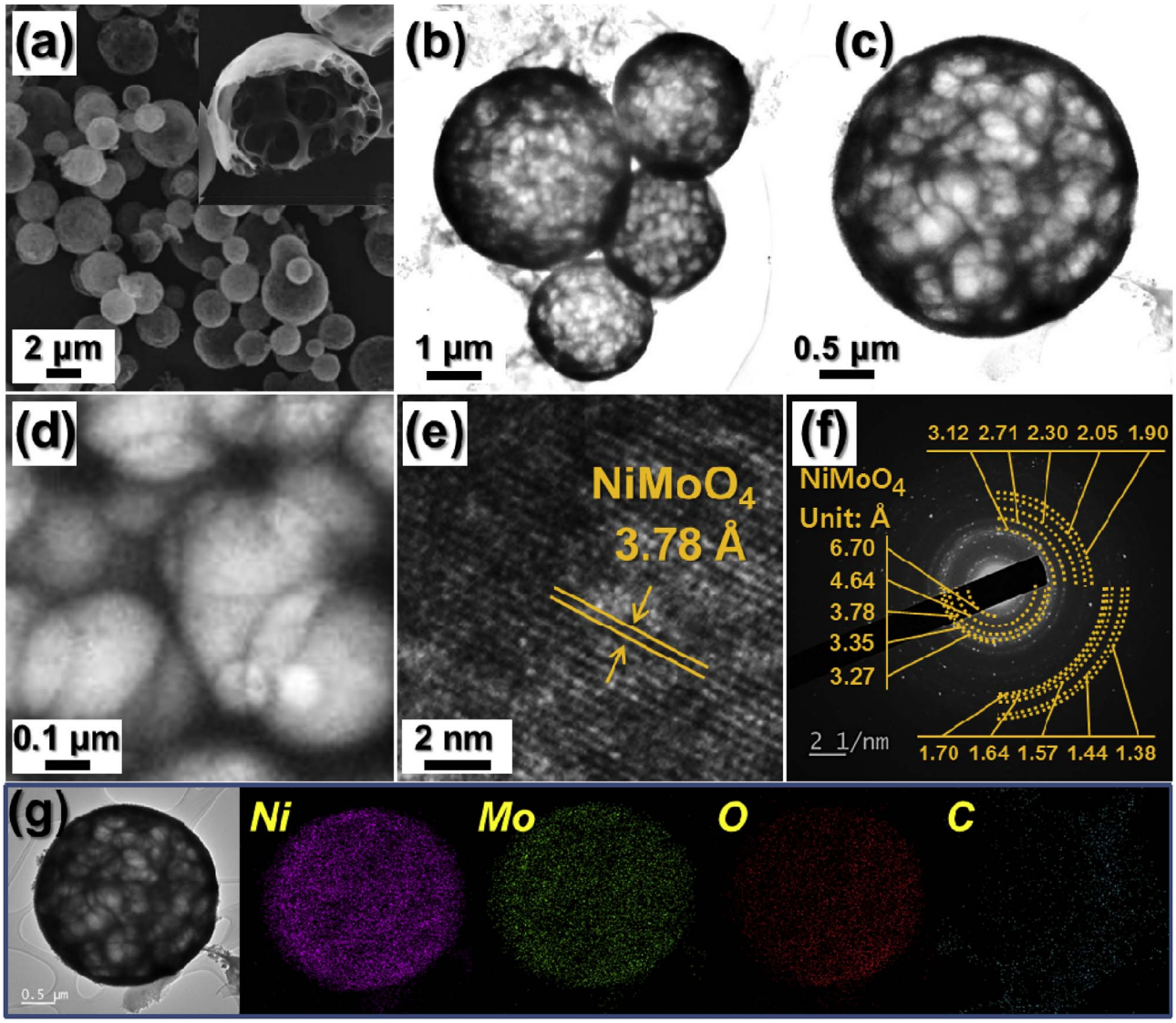

Fig. 2. Morphologies, SAED, and elemental mapping images of the multiroom-structured $NiMoO_4$ microspheres obtained at a post-treatment temperature of 400 °C: (a) SEM image, (b–d) TEM images, (e) HR-TEM image, (f) SAED pattern, and (g) elemental mapping images.

38%, respectively. In order to consider the contribution of carbon in $NiMoO_4$/C-A3 microspheres for electrochemical performance, carbon microspheres were fabricated by spray drying process using solution containing dextrin. The cycle performance of the carbon microspheres for 80 cycles at a current density of 1 A g^{-1} is shown in Fig. S6. Based on the carbon content calculated from the TG curve in Fig. S4, which is 16 wt.%, the contribution of carbon to the discharge capacity of $NiMoO_4$/C-A3 microspheres for 10th cycle was 2.2%. The capacities of $NiMoO_4$/C-A3 microspheres decreased sharply during the first 8 cycles due to their ultrafine crystallite size of $NiMoO_4$. Tarascon et al. demonstrated that transition-metal oxides showed good electrochemical properties at a certain optimum particle size [40]. However, $NiMoO_4$/C-A3 microspheres showed stable cycling performance without fluctuation of the capacities after 125 cycles due to their high structural stability during repeated lithium insertion and desertion processes. Carbon material improved the structural stability of the multiroom-structured $NiMoO_4$ microspheres. The optimum primary particle size of $NiMoO_4$-A4 microspheres post-treated at 400 °C improved their electrochemical properties even at a high current density of 1 A g^{-1}. The capacity fluctuation of $NiMoO_4$-A4 and $NiMoO_4$-A5 microspheres was attributed to the formation of thick SEI layer by partial structural damage during cycling. The minimized structural damage of $NiMoO_4$-A4 microspheres with ultrafine crystallite size resulted in the superior electrochemical properties compared to those of $NiMoO_4$/C-A3 and $NiMoO_4$-A5. In addition, a uniquely structured multicomponent metal oxide microsphere with empty nanovoids resulted in excellent cycling performance of the $NiMoO_4$-A4 microspheres. The volumetric capacities of the materials were calculated based on the electrode mass loading (1.2 mg cm^{-2}) and the average thicknesses of the composite electrode. The SEM image of electrode containing $NiMoO_4$/C-A3 was taken as a representative and shown in Fig. S7. The volumetric capacities of $NiMoO_4$/C-A3, $NiMoO_4$-A4, and $NiMoO_4$-A5 microspheres for 500^{th} cycle at a current density of 1 A g^{-1} were 613, 789, and 339 mA h cm^{-3}, respectively. The rate performance of the $NiMoO_4$-A4 microspheres consisting of ultrafine nanocrystals is shown in Fig. 6d. As the current densities increased from 0.5 to 10.0 A g^{-1}, the reversible capacities of the $NiMoO_4$-A4 microspheres decreased from 1280 to 413 mA h g^{-1}. The discharge capacities of the $NiMoO_4$-A4 microspheres recovered to 1108 mA h g^{-1} as the current density returned to 0.5 A g^{-1} after the rate performance test.

Fig. 7 displays the Nyquist plots characterized by two distinct parts: a depressed semicircle in the medium-frequency range and long tail part in the low-frequency region. The semicircle part can be used to deduce the charge transfer resistance (R_{ct}) [41–43]. R_{ct} values of

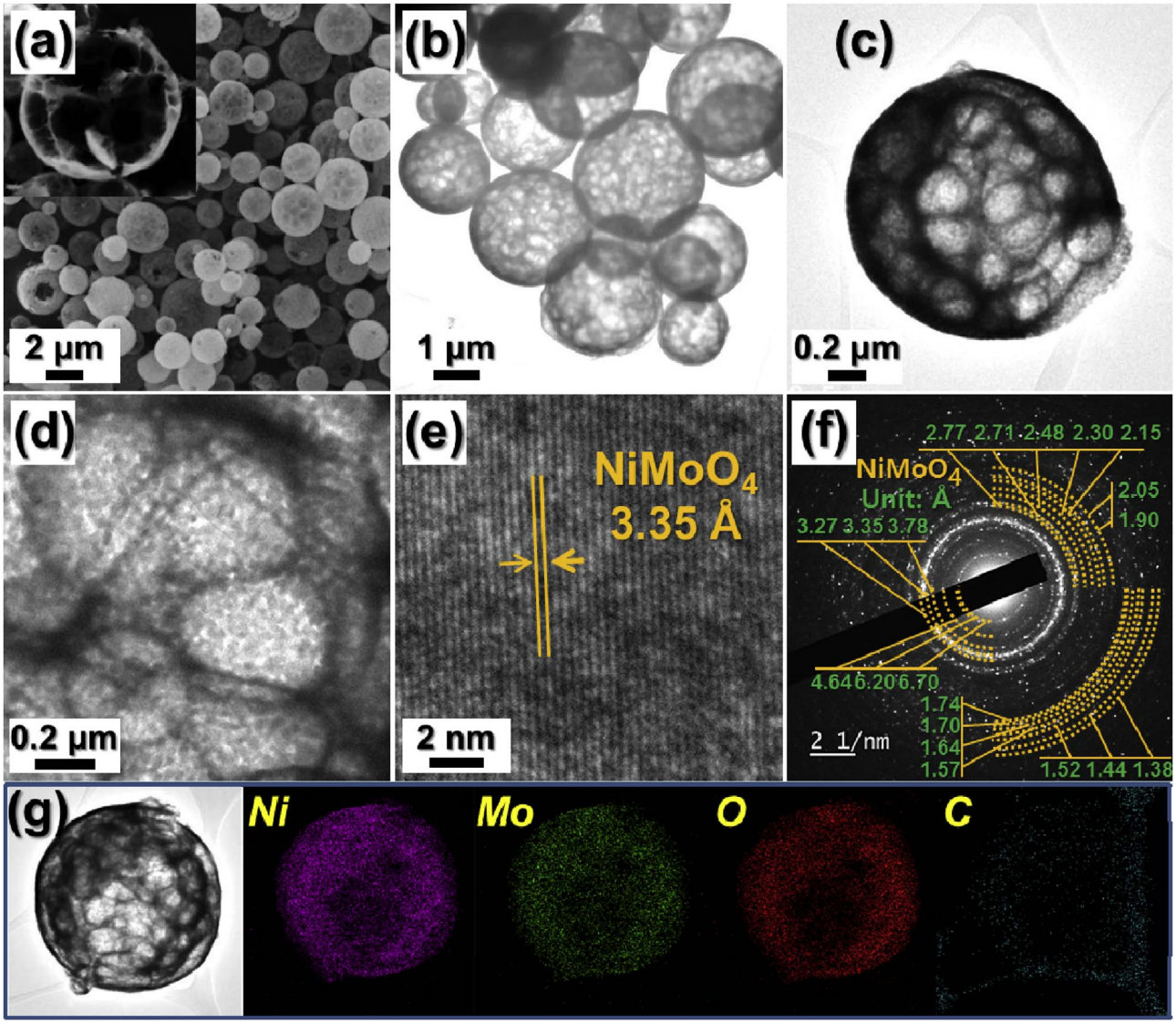

Fig. 3. Morphologies, SAED, and elemental mapping images of the multiroom-structured $NiMoO_4$ microspheres obtained at a post-treatment temperature of 500 °C: (a) SEM image, (b–d) TEM images, (e) HR-TEM image, (f) SAED pattern, and (g) elemental mapping images.

$NiMoO_4$/C-A3, $NiMoO_4$-A4, and $NiMoO_4$-A5 microspheres before cycling were calculated as 182, 133, and 135 Ω, as shown in Fig. 7a. A comparatively larger R_{ct} value for $NiMoO_4$/C-A3 could be attributed to the amorphous $NiMoO_4$ constituting the microspheres with empty nanorooms [44]. The R_{ct} value of the $NiMoO_4$-A5 microspheres after 200 cycles differed conspicuously from those of $NiMoO_4$/C-A3 and $NiMoO_4$-A4, as can be seen in Fig. 7b. The high structural damage of the $NiMoO_4$-A5 microspheres during cycling could have increased the R_{ct} value. Fig. S8 shows the impedance after the first cycle. The formation of ultrafine nanocrystals led to a decrease in the R_{ct} values of $NiMoO_4$/C-A3, $NiMoO_4$-A4, and $NiMoO_4$-A5 microspheres. The SEM images shown in Fig. S9 display the morphologies of $NiMoO_4$/C-A3, $NiMoO_4$-A4, and $NiMoO_4$-A5 microspheres after cycling. Empty nanovoids and $NiMoO_4$ frame constituting the microspheres with empty nanovoids were well observed in the SEM images after 100 cycles. The TEM image in Fig. 8 proved the structural advantage of $NiMoO_4$ microspheres with numerous empty nanovoids in way that the nanostructure remained unharmed even after 50 cycles at a high current density of 1 A g^{-1}. Fig. 8b reveals the nanovoids maintained its morphology well after cycling. Furthermore, nanocrystals constituting the main frame could be well observed. Lattice fringes in Fig. 8c reveal the existence of (110) and (021) planes of MoO_3 (JCDPS card #05-0508) and (111) plane of NiO (JCPDS card #47-1049). This further elucidates the formation of NiO and MoO_3 after charge process. To prove the superiority of the $NiMoO_4$ microspheres with empty nanovoids in lithium-ion storage, a dense-structured counterpart was prepared as well. Fig. S10a shows the morphology of the microspheres spray dried in the identical condition from a solution without dextrin. Necking between the particles occurred due to low stability of the spray-dried product without dextrin under high humidity. The microspheres were subsequently oxidized at 400 °C to form dense-structured microspheres, as shown in Fig. S10b. The dense-structured $NiMoO_4$ microspheres had low first discharge and charge capacities at 1 A g^{-1}, as shown in Fig. S11a, of 1033 and 819 mA h g^{-1}, respectively. In addition, the discharge capacities of the dense-structured $NiMoO_4$ microspheres decreased steadily during 100 cycles, as shown in Fig. S11b. The discharge capacity at the 100th cycle was 170 mA h g^{-1}, and the capacity retention measured from the second cycle was 20.7%. The existence of an empty nanovoid within the microspheres proved effective when applied as an anode material for lithium-ion storage.

4. Conclusions

In the current work, electrochemical properties of $NiMoO_4$

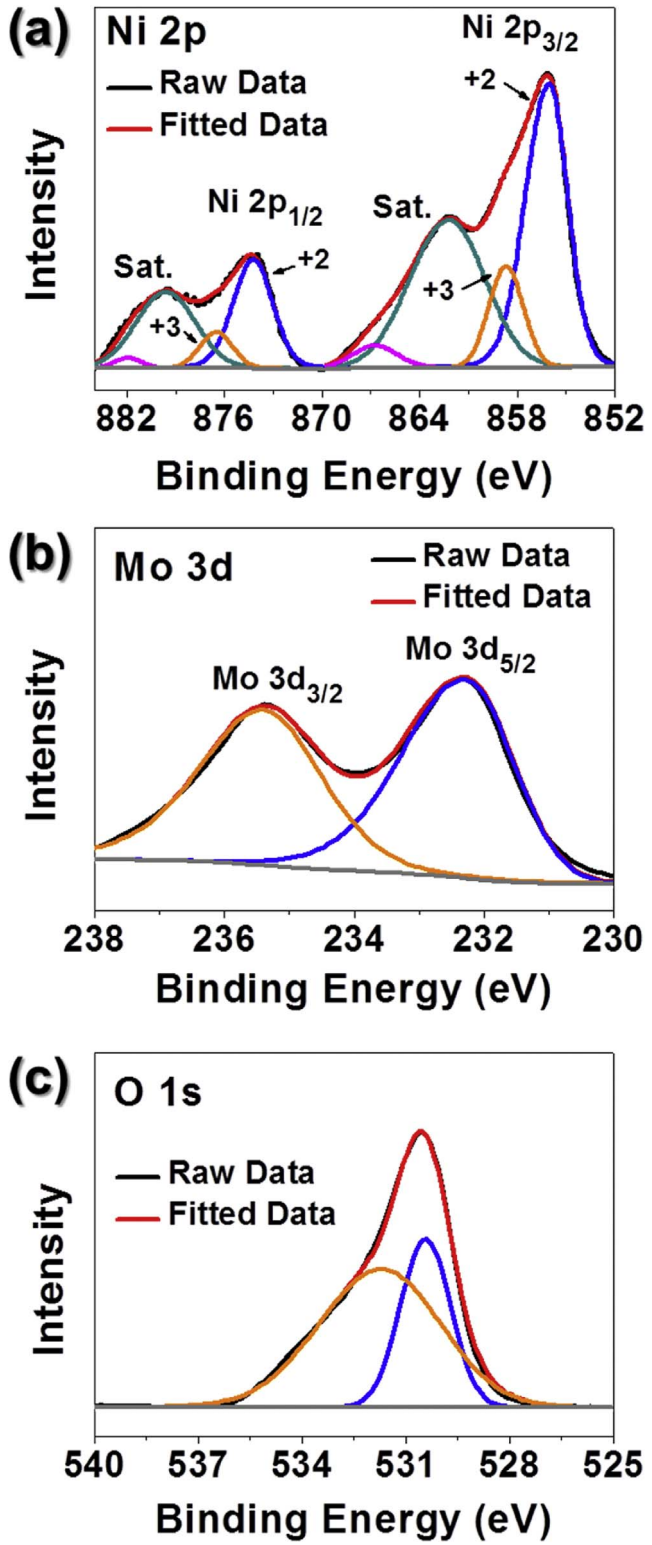

Fig. 4. XPS spectra of the multiroom-structured $NiMoO_4$ microspheres ($NiMoO_4$-A4): (a) Ni 2p, (b) Mo 3d, and (c) O 1s.

microspheres with empty nanovoids as an anode material for LIBs were evaluated. A scalable pilot-scale spray drying process was used for producing microspheres containing phase segregated metal salts and dextrin that become $NiMoO_4$ frame and well-distributed empty nanovoids after a simple calcination step in air. Combining the excellent electrochemical nature of Ni and high electrical conductivity of Mo, together with multiple valence states of the transition metal molybdate,

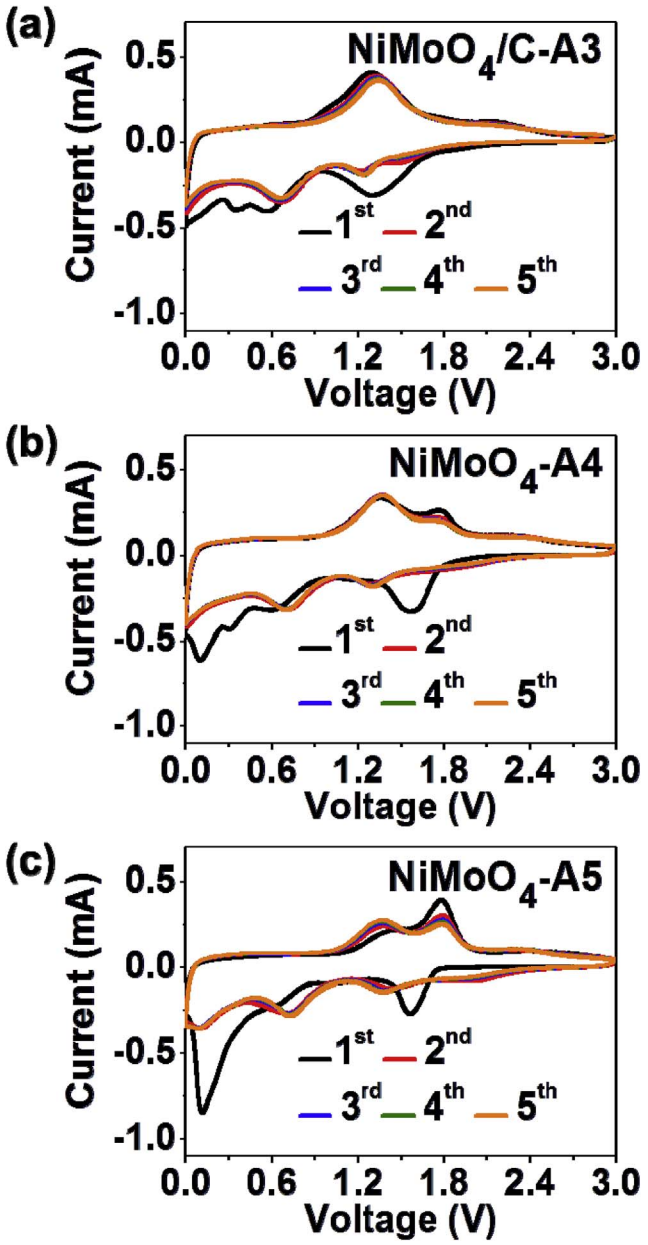

Fig. 5. CV curves of the multiroom-structured $NiMoO_4$ microspheres: (a) $NiMoO_4$/C-A3, (b) $NiMoO_4$-A4, and (c) $NiMoO_4$-A5.

$NiMoO_4$ microspheres exhibited excellent electrochemical properties. The effect of empty nanovoids within the microspheres was examined by comparing battery performance with $NiMoO_4$ microspheres with dense structure, synthesized by a spray drying process from a solution without dextrin and the subsequent calcination step. $NiMoO_4$ microspheres with empty nanovoids were superior to dense-structured $NiMoO_4$ microspheres in both capacity and cycle performance. Therefore, we believe that the concept of $NiMoO_4$ microspheres with empty nanovoids in this study could be tailored and used in various applications.

Acknowledgment

This work was supported by the National Research Foundation of Korea grant funded by the Korea government(MSIP) (NRF-2017R1A2B2008592). This research was supported by Basic Science Research Program through the National Research Foundation of Korea funded by the Ministry of Science, ICT and Future Planning (NRF-

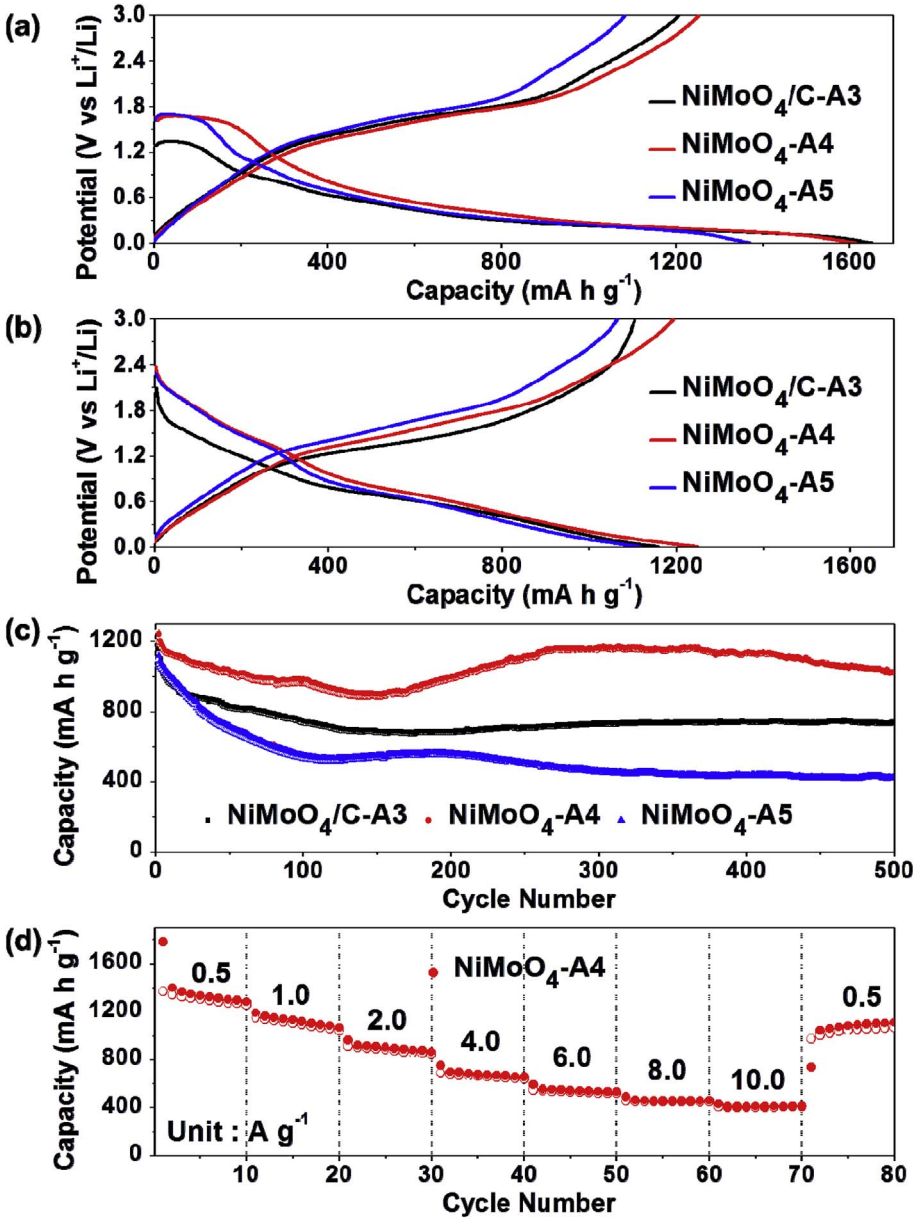

Fig. 6. Electrochemical properties of the multiroom-structured $NiMoO_4$ microspheres: (a) first charge-discharge curves, (b) second charge-discharge curves and (c) cycling performances at a current density of 1 A g^{-1}, and (d) rate performance of $NiMoO_4$-A4.

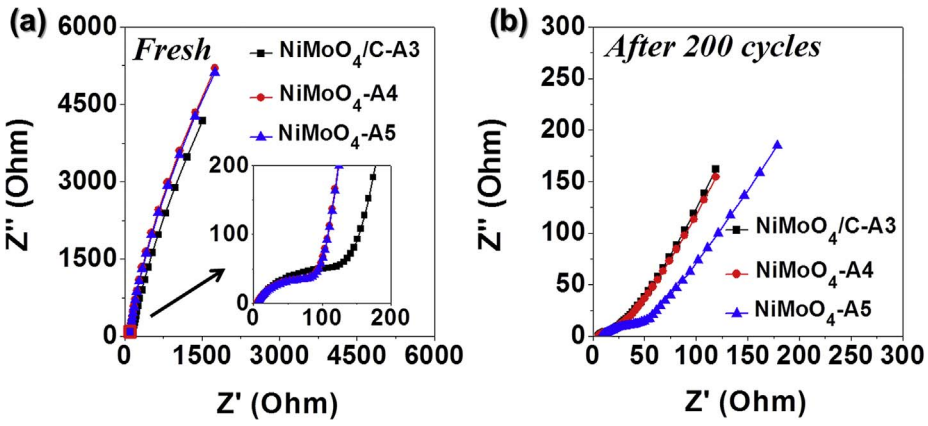

Fig. 7. Nyquist plots of $NiMoO_4$ microspheres: (a) before and (b) after 200 cycles.

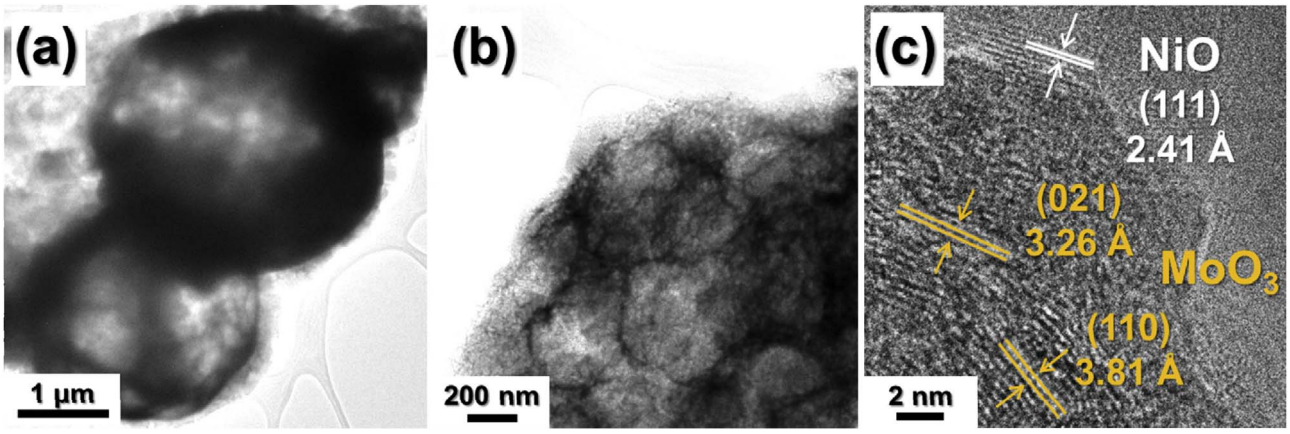

Fig. 8. (a,b) TEM images and (c) HR-TEM image of $NiMoO_4$-A4 microspheres after 50 cycles.

2017R1A4A1014806, NRF-2017R1A2B3011676).

Appendix A. Supplementary data

Supplementary data related to this article can be found at http://dx.doi.org/10.1016/j.jpowsour.2018.01.050.

References

[1] H. Li, Y. Su, W. Sun, Y. Wang, Carbon nanotubes rooted in porous ternary metal sulfide@N/S-doped carbon dodecahedron: bimetal-organic-frameworks derivation and electrochemical application for high-capacity and long-life lithium-ion batteries, Adv. Funct. Mater. 22 (2016) 8345–8353.
[2] M. Yan, G. Zhang, Q. Wei, X. Tian, K. Zhao, Q. An, L. Zhou, Y. Zhao, C. Niu, W. Ren, L. He, L. Mai, In operando observation of temperature-dependent phase evolution in lithium-incorporation olivine cathode, Nano Energy 22 (2016) 406–413.
[3] Y.J. Hong, M.Y. Son, Y.C. Kang, One-pot facile synthesis of double-shelled SnO_2 yolk-shell-structured powders by continuous process as anode materials for Li-ion batteries, Adv. Mater. 25 (2013) 2279–2283.
[4] S.K. Park, S.H. Yu, N. Pinna, S. Woo, B. Jang, Y.H. Chung, Y.H. Cho, Y.E. Sung, Y. Piao, A facile hydrazine-assisted hydrothermal method for the deposition of monodisperse SnO_2 nanoparticles onto graphene for lithium ion batteries, J. Mater. Chem. 22 (2012) 2520–2525.
[5] E.M. Lotfabad, J. Ding, K. Cui, A. Kohandehghan, W.P. Kalisvaart, M. Hazelton, D. Mitlin, High-density sodium and lithium ion battery anodes from banana peels, ACS Nano 8 (2014) 7115–7129.
[6] Y. Chen, B. Song, X. Tang, L. Lu, J. Xue, Ultrasmall Fe_3O_4 nanoparticle/MoS_2 nanosheet composites with superior performances for lithium ion batteries, Small 10 (2014) 1536–1543.
[7] X. Zhou, L.J. Wan, Y.G. Guo, Binding SnO_2 nanocrystals in nitrogen-doped graphene sheets as anode materials for lithium-ion batteries, Adv. Mater. 25 (2013) 2152–2157.
[8] Y. Chen, B. Song, M. Li, L. Lu, J. Xue, Fe_3O_4 Nanoparticles embedded in uniform mesoporous carbon spheres for superior high-rate battery applications, Adv. Funct. Mater. 24 (2014) 319–326.
[9] L. Yu, J.F. Yang, X.W.D. Lou, Formation of CoS_2 nanobubble hollow prisms for highly reversible lithium storage, Angew. Chem. Int. Ed. 55 (2016) 13422–13426.
[10] H. Zhao, Y. Li, Z. Zhu, J. Lin, Z. Tian, R. Wang, Structural and electrochemical characteristics of $Li_{4-x}Al_xTi_5O_{12}$ as anode material for lithium-ion batteries, Electrochim. Acta 53 (2008) 7079–7083.
[11] X. Wang, H. Zhang, Y. Xu, C. Chen, H. Yuan, Y. Wang, CTAB-assisted multiwalled carbon nanotube-loaded $NaFe_2Mn(PO_4)_3$ materials as high performance cathodes for sodium-ion batteries, RSC Adv. 6 (2016) 67986–67991.
[12] Z. Ju, E. Zhang, Y. Zhao, Z. Xing, Q. Zhuang, Y. Qiang, Y. Qian, One-pot hydrothermal synthesis of $FeMoO_4$ nanocubes as an anode material for lithium-ion batteries with excellent electrochemical performance, Small 11 (2015) 4753–4761.
[13] Z. Zhang, W. Li, T.W. Ng, W. Kang, C.S. Lee, W. Zhang, Iron (II) molybdate ($FeMoO_4$) nanorods as a high-performance anode for lithium ion batteries: structural and chemical evolution upon cycling, J. Mater. Chem. A 3 (2015) 20527–20534.
[14] C.T. Cherian, M.V. Reddy, S.C. Haur, B.V.R. Chowdari, Interconnected network of $CoMoO_4$ submicrometer particles as high capacity anode material for lithium ion batteries, ACS Appl. Mater. Interfaces 5 (2013) 918–923.
[15] Y. Chen, B. Liu, W. Jiang, Q. Liu, J. Liu, J. Wang, H. Zhang, X. Jing, Coaxial three-dimensional $CoMoO_4$ nanowire arrays with conductive coating on carbon cloth for high- performance lithium ion battery anode, J. Power Sources 300 (2015) 132–138.
[16] B. Wang, S. Li, X. Wu, W. Tian, J. Liu, M. Yu, Integration of network-like porous $NiMoO_4$ nanoarchitectures assembled with ultrathin mesoporous nanosheets on three- dimensional graphene foam for highly reversible lithium storage, J. Mater. Chem. A 3 (2015) 13691–13698.
[17] K. Xiao, L. Xia, G. Liu, S. Wang, L.X. Ding, H. Wang, Honeycomb-like $NiMoO_4$ ultrathin nanosheet arrays for high-performance electrochemical energy storage, J. Mater. Chem. A 3 (2015) 6128–6135.
[18] B. Wang, S. Li, X. Wu, J. Liu, W. Tian, Hierarchical $NiMoO_4$ nanowire arrays supported on macroporous graphene foam as binder-free 3D anodes for high-performance lithium storage, Phys. Chem. Chem. Phys. 18 (2016) 908–915.
[19] J.S. Cho, Y.J. Hong, Y.C. Kang, Design and synthesis of bubble-nanorod-structured Fe_2O_3–carbon nanofibers as advanced anode material for Li-ion batteries, ACS Nano 9 (2015) 4026–4035.
[20] S. Li, A. Li, R. Zhang, Y. He, Y. Zhai, L. Xu, Hierarchical porous metal ferrite ball-in-ball hollow spheres: general synthesis, formation mechanism, and high performance as anode materials for Li-ion batteries, Nano Res. 7 (2014) 1116–1127.
[21] L. Shen, L. Yu, X.Y. Yu, X. Zhang, X.W.D. Lou, Self-templated formation of uniform $NiCo_2O_4$ hollow spheres with complex interior structures for lithium-ion batteries and supercapacitors, Angew. Chem. Int. Ed. 54 (2015) 1868–1872.
[22] Y.N. Ko, S.B. Park, Y.C. Kang, Design and fabrication of new nanostructured SnO_2-carbon composite microspheres for fast and stable lithium storage performance, Small 10 (2014) 3240–3245.
[23] S.H. Choi, Y.N. Ko, J.K. Lee, Y.C. Kang, 3D MoS_2–graphene microspheres consisting of multiple nanospheres with superior sodium ion storage properties, Adv. Funct. Mater. 25 (2015) 1780–1788.
[24] J.S. Xu, Y.J. Zhu, Monodisperse Fe_3O_4 and γ-Fe_2O_3 magnetic mesoporous microspheres as anode materials for lithium-ion batteries, ACS Appl. Mater. Interfaces 4 (2012) 4752–4757.
[25] J.S. Park, Y.C. Kang, Multicomponent (Mo, Ni) metal sulfide and selenide microspheres with empty nanovoids as anode materials for Na-ion batteries, J. Mater. Chem. A 5 (2017) 8616–8623.
[26] Y. Xu, G. Jian, Y. Liu, Y. Zhu, M.R. Zachariah, C. Wang, Superior electrochemical performance and structure evolution of mesoporous Fe_2O_3 anodes for lithium-ion batteries, Nano Energy 3 (2014) 26–35.
[27] J.S. Cho, J.M. Won, J.K. Lee, Y.C. Kang, Design and synthesis of multiroom-structured metal compounds–carbon hybrid microspheres as anode materials for rechargeable batteries, Nano Energy 26 (2016) 466–478.
[28] F. Iskandar, A.B.D. Nandiyanto, K.M. Yun, C.J. Hogan, K. Okuyama, P. Biswas, Enhanced photocatalytic performance of brookite TiO_2 macroporous particles prepared by spray drying with colloidal templating, Adv. Mater. 19 (2007) 1408–1412.
[29] G.D. Park, J.S. Cho, Y.C. Kang, Sodium-ion storage properties of nickel sulfide hollow nanospheres/reduced graphene oxide composite powders prepared by a spray drying process and the nanoscale Kirkendall effect, Nanoscale 7 (2015) 16781–16788.
[30] F. Iskandar, M. Abdullah, K. Okuyama, In situ production of spherical silica particles containing self-organized mesopores, Nano Lett. 1 (2001) 231–234.
[31] J.H. Kim, Y.C. Kang, Electrochemical properties of micron-sized, spherical, meso- and macro-porous Co_3O_4 and CoO–carbon composite powders prepared by a two-step spray drying process, Nanoscale 6 (2014) 4789–4795.
[32] J. Ma, Z. Fang, Y. Yan, Z. Yang, L. Gu, Y.S. Hu, H. Li, Z. Wang, X. Huang, Novel large-scale synthesis of a C/S nanocomposite with mixed conducting networks through a spray drying approach for Li–S batteries, Adv. Energy Mater. 5 (2015) 1500046.
[33] J.S. Cho, S.Y. Lee, H.S. Ju, Y.C. Kang, Synthesis of NiO nanofibers composed of hollow nanospheres with controlled sizes by the nanoscale Kirkendall diffusion process and their electrochemical properties, ACS Appl. Mater. Interfaces 7 (2015) 25641–25647.
[34] J.S. Cho, J.M. Won, J.-H. Lee, Y.C. Kang, Synthesis and electrochemical properties of spherical and hollow-structured NiO aggregates created by combining the Kirkendall effect and Ostwald ripening, Nanoscale 7 (2015) 19620–19626.
[35] P. Meduri, E. Clark, J.H. Kim, E. Dayalan, G.U. Sumanasekera, M.K. Sunkara, MoO_{3-x} nanowire arrays as stable and high-capacity anodes for lithium ion batteries, Nano Lett. 12 (2012) 1784–1788.

[36] N.N. Leyzerovich, K.G. Bramnik, T. Buhrmester, H. Ehrenberg, H. Fuess, Electrochemical intercalation of lithium in ternary metal molybdates $MMoO_4$ (M: Cu, Zn, Ni and Fe), J. Power Sources 127 (2004) 76–84.
[37] J.H. Ahn, G.D. Park, Y.C. Kang, J.H. Lee, Phase-pure β-$NiMoO_4$ yolk-shell spheres for high-performance anode materials in lithium-ion batteries, Electrochim. Acta 174 (2015) 102–110.
[38] Y. Sun, J. Wang, B. Zhao, R. Cai, R. Ran, Z. Shao, Binder-free α-MoO_3 nanobelt electrode for lithium-ion batteries utilizing van der Waals forces for film formation and connection with current collector, J. Mater. Chem. A 1 (2013) 4736–4746.
[39] F. Ma, A. Yuan, J. Xu, P. Hu, Porous α-MoO_3/MWCNT nanocomposite synthesized via a surfactant-assisted solvothermal route as a lithium-ion-battery high-capacity anode material with excellent rate capability and cyclability, ACS Appl. Mater. Interfaces 7 (2015) 15531–15541.
[40] S. Grugeon, S. Laruelle, R. Herrera-Urbina, L. Dupont, P. Poizot, J.M. Tarascon, Particle size effects on the electrochemical performance of copper oxides toward lithium, J. Electrochem. Soc. 148 (2001) A285–A292.
[41] Y. Wang, Z. Huang, Y. Wang, A new approach to synthesize MoO_2@C for high-rate lithium ion batteries, J. Mater. Chem. A 3 (2015) 21314–21320.
[42] K. Lee, S.Y. Shin, Y.S. Yoon, Fe_3O_4 nanoparticles on MWCNTs backbone for lithium ion batteries, J. Korean Ceram. Soc. 53 (2016) 376–380.
[43] C. Dong, L. Xu, Cobalt-and cadmium-based metal-organic frameworks as high-performance anodes for sodium ion batteries and lithium ion batteries, ACS Appl. Mater. Interfaces 9 (2017) 7160–7168.
[44] J. Ma, X. Zhang, K. Chen, G. Li, X. Han. Wang, Morphology-controlled synthesis of hematite hierarchical structures and their lithium storage performances, J. Mater. Chem. A 1 (2013) 5545–5553.